Phase transformations in thin iron oxide films:
Spectromicroscopic study of velocity and shape of the reaction fronts

F. Genuzio, A. Sala, Th. Schmidt, D. Menzel, H.-J. Freund

Fritz-Haber-Institute of the Max-Planck-Society, Department of Chemical Physics, Faradayweg 4-6, 14195 Berlin, Germany

Dedicated to Gabor Somorjai at the occasion of his 80th birthday

Combining low energy electron microscopy (LEEM) with low energy electron diffraction (LEED) and x-ray photoemission electron microscopy (XPEEM) we studied the phase transformations between Fe_3O_4, γ-Fe_2O_3, and α-Fe_2O_3, grown as 10 nm thin oxide films on Pt(111) and Ag(111) single crystals. These transformations occur as moving reaction fronts in most cases, the shapes and velocities of which show strong dependences on temperature and oxygen pressure, but also on defects like step bunches of the supporting substrate and domain boundaries in the initial oxide film. While the non-uniform moving fronts make a quantitative analysis difficult, we have extracted approximate values for the average front velocities. We discuss these as well as the qualitative information on the non-uniform fronts in terms of the known geometric situations and the likely motional steps.

Keywords: Iron oxides, phase transformation, moving reaction fronts, activation energy, LEEM, XPEEM

1   Introduction

Iron oxides are in the focus of scientific investigations due to their natural abundance, their stability and easy interconversion, and because of their many applications in technology, e.g. in catalysis and magnetic devices.[1-4] Considerable efforts have been expended to understand their physical and chemical properties. Thin films, in particular of Fe_3O_4 (magnetite) and α-Fe_2O_3 (hematite), have been used to model bulk materials under well-defined experimental conditions as well as to clarify the influences of limited thickness and variable support.

Despite the large number of studies related to the reversible transformations between different Fe-oxide phases, there is a lack of microscopic studies which visualize directly the movement of reaction fronts in real time, i.e. to probe the local kinetics of the reaction. It is well known that the local velocity and concomitantly the shape of the moving solid-solid phase boundary is not only influenced by the gradient of the chemical potential, but also by local stress, point or line defects at the parent/product interface, as well as their relative crystalline orientations.[5-12] The interplay between thermodynamic and elastic driving forces controls the morphology of the transition at the phase boundary.

In a recent publication [13] we described a systematic study of the reversible transition $Fe_3O_4 \leftrightarrow \alpha\text{-}Fe_2O_3$ in supported thin films. Our experiments underlined that the transformations are heterogeneous, i.e. the film consists of two types of phase domains separated by moving reaction fronts. The transformation is strongly affected by the choice of the supporting substrate (in our case Pt(111) and Ag(111)). In the present work we describe detailed investigations of the kinetics of the $Fe_3O_4|\alpha\text{-}Fe_2O_3$ and $\gamma\text{-}Fe_2O_3|\alpha\text{-}Fe_2O_3$ phase boundaries including the characterization of the shape of the moving front under different experimental conditions. The experiments take advantage of the real time acquisition rate and the nanometer resolution of the SMART microscope, combined with structural (LEED) and spectroscopic information (XPEEM and spatially resolved XPS).[14-18] Similar experimental systems have been successfully applied to the study of moving reaction fronts on surfaces and thin films.[19-25]

The phase transformation between $Fe_3O_4 \leftrightarrow \alpha\text{-}Fe_2O_3$ involves both <u>compositional</u> (i.e. changing the ratio of Fe:O from 3:4 to 2:3**)** and <u>structural</u> changes (i.e. from inverse spinel to corundum and vice versa). However, composition and structure can change independently from each other. If the composition changes without structural modification, Fe_3O_4 oxidizes to $\gamma\text{-}Fe_2O_3$, both having the same crystal structure but with Fe vacancies for the latter. [26-28] On the other hand, the (irreversible) transformation from $\gamma\text{-}Fe_2O_3$ to $\alpha\text{-}Fe_2O_3$ is a purely structural phase transformation, between allotropes.

We have investigated the reactions:

- $Fe_3O_4 \leftrightarrow \alpha\text{-}Fe_2O_3$: direct compositional and structural transformation in both directions

- $\gamma\text{-}Fe_2O_3 \rightarrow \alpha\text{-}Fe_2O_3$: pure structural transformation (irreversible).

- $\gamma\text{-}Fe_2O_3 \rightarrow Fe_3O_4$: pure compositional transformation

By direct observation of the propagation of the phase transformation, we measured the local reaction front velocity. In the $Fe_3O_4 \rightarrow \alpha\text{-}Fe_2O_3$ transformation two different morphological regimes were

identified and could be correlated to well-defined experimental conditions (temperature and O_2 pressure). The measured velocities of the transformation front covered a range from less than 1 nm/s to 200 nm/s, depending on the sample temperature, oxygen pressure, and substrate. Therefore, we had to optimize the microscope magnification and the acquisition time to follow the processes with sufficient accuracy. From the temperature dependence of the various transformation velocities we derived effective activation energies for the processes involved in the transformation.

2 Overview of structures and transitions

Fe_3O_4 (magnetite), α-Fe_2O_3 (hematite), and γ-Fe_2O_3 (maghemite) are the materials investigated in our experiments. Their different crystal structures have been discussed in detail in references.[4, 29] Here we give just a brief overview.

α-Fe_2O_3 crystallizes in the corundum structure with a hexagonal unit cell. Along the [0001] direction the O anions form a close-packed hcp sub-lattice with ABAB stacking. The Fe^{3+} species between these layers are arranged in honeycomb ($\sqrt{3}x\sqrt{3}$)R30° like layers. On an area of 12 O anions there are 8 Fe cations.

Fe_3O_4 crystallizes in the inverse spinel structure. The O anions form a close-packed fcc sub-lattice with Fe^{2+} and Fe^{3+} cations located in the interstitial sites. Along the [111] axis of Fe_3O_4, the hexagonal O planes form a cubic ABC stacking sequence. The vertical packing density of the O planes is similar to that of the O planes of α-Fe_2O_3. Between the close-packed planes of oxygen ions either one Kagomé or three hexagonal (mix-trigonal) Fe layers alternate. Both ion sub-lattices are arranged in a (2x2)-like fashion on the close-packed oxygen layer. Here, 9 Fe cations are arranged on an area of 12 O anions.

γ-Fe_2O_3 (maghemite) is a metastable phase with a cubic crystal structure close to the Fe_3O_4 magnetite structure. When Fe_3O_4 is oxidized to γ-Fe_2O_3, arbitrarily distributed cation vacancies are created at octahedral interstitials resulting in only Fe^{3+} cations. The so-called "non-stoichiometric magnetite" $Fe_{(3-\delta)}O_4$ (with $0 < \delta < ⅓$) corresponds to the situation where only part of these vacancies are formed ($\delta = ⅓$ corresponds to maghemite).

The phase transformation $Fe_3O_4 \leftrightarrow \alpha$-$Fe_2O_3$ occurs as a moving front between two domains (see also [13]), i.e. it is a <u>heterogeneous</u> transformation. This solid state reaction involves the "simultaneous" change of the crystal <u>composition</u> and <u>structure</u>. If the two processes do not occur simultaneously, we have the purely compositional transformation $Fe_3O_4 \rightarrow \gamma$-$Fe_2O_3$, or the purely structural γ-$Fe_2O_3 \rightarrow \alpha$-$Fe_2O_3$.

Under "standard" oxidation conditions (bulk crystal, external O_2 pressure), the compositional change from Fe_3O_4 to γ-Fe_2O_3 occurs by Fe diffusion through the bulk to the surface. Under the gradient of chemical potential μ_{O2} the Fe at the surface is oxidized by adsorbed oxygen [10, 28]. The activation energy for this process was measured to $\Delta E_A \approx 20$ kcal/mol, corresponding to 0.87 eV.[30-32]

The structural transformation from the spinel phase γ-Fe_2O_3 to the corundum phase α-Fe_2O_3 requires the re-stacking of the oxygen layers from fcc to hcp, and the rearrangement of the Fe cations. This process is believed to progress through rigid O layers shifting against each other which induces the simultaneous adjustment of cations in the new structure.[10, 33, 34] A "synchro-shear mechanism" for the $\gamma \rightarrow \alpha$ (in Fe_2O_3) has been proposed in ref. [35]; similar mechanisms have also been suggested for the $\Theta \rightarrow \alpha$ transition in Al_2O_3[36, 37] and for the reverse transformation (i.e. α-$Fe_2O_3 \rightarrow Fe_3O_4$) [38].

The process follows the topotactic relationship between the crystalline orientations in the two structures:

- $(111)_{spinel}//(0001)_{corundum}$
- $[\bar{1}10]_{spinel}//[\bar{1}100]_{corundum}$

and combines two simultaneous processes:

a. the fcc $\rightarrow$ hcp transformation of the O plane stacking;

b. the rearrangement of the Fe atoms in the Fe layers into the new structure.

In γ-Fe_2O_3 (fcc) and α-Fe_2O_3 (hcp) the stacking of the oxygen layers can be represented as ABCABC and ABABABA, respectively. Consequently, the fcc|hcp interface between the two oxide structures consists of repeated units of in plane stacking faults of the types: A|C, A|B, B|A and C|B (see Figure 1). In the (111) and (0001) direction, neighboring oxygen planes are separated by Fe layers: alternatingly Kagomé and mix-trigonal in γ-Fe_2O_3; honeycomb in α-Fe_2O_3. During the fcc $\rightarrow$ hcp transformation, the stress arising at the fcc|hcp interface is released by transferring the interfacial fcc O atoms into the "correct" (hcp) position, resulting in the propagation of the hcp interface by one atomic distance. The displacement for each oxygen atom is $a_0/\sqrt{3}$, where a_0 is the interatomic O-O distance in the un-deformed O layer; the direction of the displacement is the one which eliminates the planar stacking fault (Figure 1)
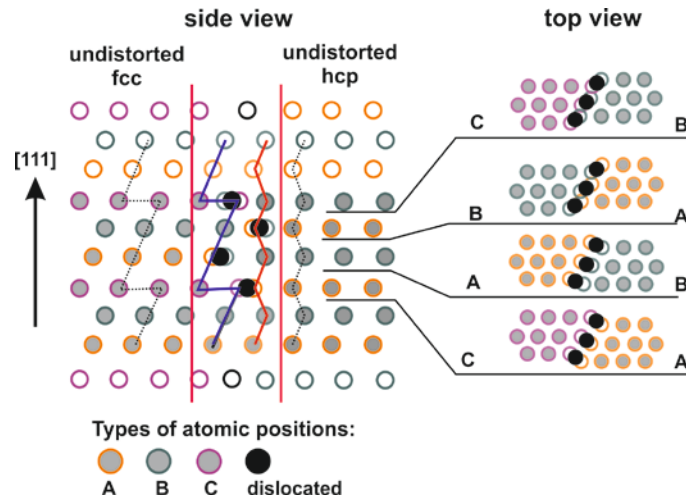
Figure 1: Schematic view of a simplified interface between fcc and hcp structures; filled black circles denote dislocated atoms assuming an intermediate position at the interface. For simplicity the layers are assumed to be perfectly aligned in the vertical stacking.

Simultaneous with the oxygen plane displacement, the Fe atoms rearrange from the spinel (mix-trigonal and Kagomé) into the new honeycomb structure, by short range interlayer Fe diffusion; this short range diffusion process is similar to the diffusion of Fe involved in the grain/anti-phase boundaries movement in Fe_3O_4[39].

The Fe layer rearrangement drives the modification of the crystal unit cell from (2x2) to (√3x√3)R30° with respect to the oxygen layers (Figure 2a). This difference in superstructures accounts for the structural contrast in LEEM, so that the propagating reaction fronts can be observed. According to the model proposed in ref. [35], the Kagomé transforms directly into the honeycomb layer, while the mix-trigonal layer first transforms to the Kagomé layer and subsequently to honeycomb.

In the transformation between Fe_3O_4 and α-Fe_2O_3, we notice that 1/9 of Fe atoms in Fe_3O_4 have to be removed, forming arbitrarily distributed vacancies in the crystal lattice. Once the vacancies exist, the same structural transformation mechanism as described above can be applied. If the vacancy formation is limited to (or occurs preferentially at) the phase boundary, the Fe_3O_4 composition far from the reaction front can be assumed to be stoichiometric, i.e. the chemical composition of the inverse spinel Fe_3O_4 parent phase differs from the one of the corundum product. This means that during the ongoing oxidation reaction, the chemical composition of the parent phase needs to be continuously adjusted close to the advancing reaction front.

Most likely, the transition occurs in two steps: first the compositional (Fe_3O_4 → γ-Fe_2O_3) and subsequently the structural change (γ-Fe_2O_3 → α-Fe_2O_3). However, the initial Fe_3O_4 film possibly does not entirely convert to γ-Fe_2O_3 but only in a smaller range at the boundary, directly followed by the transformation to α-Fe_2O_3. The transformation front would then be spatially extended and consist of two phase boundaries (Fe_3O_4|γ-Fe_2O_3 and γ-Fe_2O_3|α-Fe_2O_3). Because the intermediate γ-Fe_2O_3 phase

covers only a small fraction of the entire surface, we call this transformation still a "direct" conversion from Fe_3O_4 to α-Fe_2O_3.

3   Experimental methods and procedures

The sample preparation and the experiments were carried out in the SMART spectro-microscope. This aberration-corrected and energy-filtered LEEM-PEEM system combines spectroscopy (XPS, NEXAFS), microscopy (LEEM, PEEM, XPEEM), and diffraction techniques (LEED, SPA-LEED) for comprehensive surface characterization with high lateral resolution. The high acquisition rate allows the *real time* observation of surface processes like growth, chemical reaction, and phase transitions. [14-18].

The system has a base pressure of 1×10^{-10} mbar, but can also be operated in an oxygen pressure ranging up to 10^{-5} mbar when oxygen (99.999% purity) is dosed by a leak valve directly into the main chamber. The supporting substrates were Ag(111) and Pt(111) single crystals, mounted on a commercial ELMITEC sample holder which can be heated up to 2000 K from the back side either by radiation from a filament or by electron bombardment. The temperature was measured with an absolute accuracy of about 10 K by a W26%Re/W5%Re thermocouple, spot-welded to the crystal support. Iron (99.995% purity, Alfa Aesar) was vapor deposited using a commercial evaporator (Omicron EFM3 with ion suppressor) pointing towards the sample under grazing incidence of 20°.

All techniques used in our investigations are surface sensitive, with a probing depth of few atomic layers. Therefore, we could not study the vertical extent of the transformations beyond this depth. However, we assume that the stable film structure, observed at the surface, represents the entire oxide film thickness of about 10 nm, following the arguments already discussed in ref. [13].

Iron oxide thin films were grown on clean Pt(111) and Ag(111) single crystal substrates by repeated cycles of iron deposition and oxidation at elevated temperature.[13, 29, 40] Films with mixed Fe_3O_4(111) and α-Fe_2O_3(0001) phases were prepared following the procedure recently described in ref. [13]. Under our preparation conditions the α-Fe_2O_3(0001) surface is always bi-phase terminated.[41-43] A uniform γ-Fe_2O_3(111) phase was obtained by low temperature oxidation (T < 620 K, p_{O2}= 3 10^{-5} mbar for 10 min) of the Fe_3O_4 film with subsequent cooling down, during which the oxygen pressure was not reduced before reaching 450 K.[13, 40] The co-existence of the γ- and the α-Fe_2O_3 phases was produced by flashing a γ-Fe_2O_3 film under UHV condition (T = 850 K) to induce a partial structural transformation.
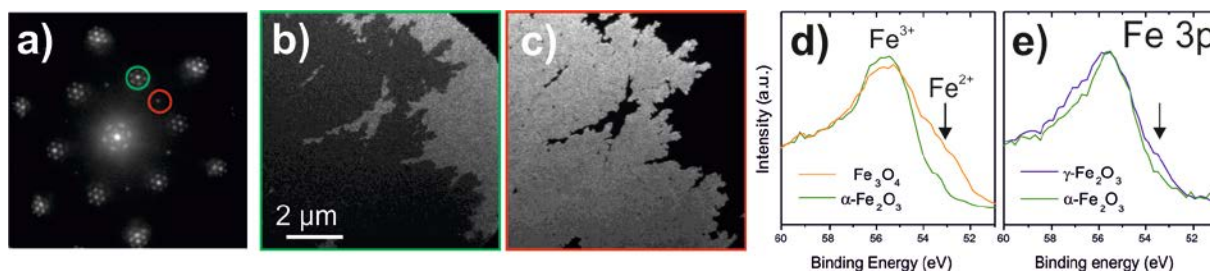
Figure 2: Phase identification by LEED (a), darkfield LEEM (b-c) and local XPS (d-e) of iron oxide films containing mixed phases. The LEED pattern is a superposition of spinel and corundum structures. The darkfield images b) and c) use the green and red labelled LEED spots, identifying the corundum and spinel structures as bright areas, respectively. Electron energy in a-c) is 38 eV. The two local Fe 3p XPS are taken at mixed spinel/corundum films, consisting of Fe_3O_4 and α-Fe_2O_3 (Fig. d) and γ-Fe_2O_3 and α-Fe_2O_3 (Fig. e). Fe_3O_4 is identified by the presence of the Fe^{2+} signal.

The phase identification is based on the crystal structure and the stoichiometry of the different Fe-oxides, combining darkfield LEEM, LEED, and XPEEM. The corundum structure of the α-Fe_2O_3(0001) film can be easily distinguished from the spinel structures, Fe_3O_4 (111) and α-Fe_2O_3, by the specific diffraction patterns (LEED) (Figure 2a). The two spinel oxides, in the (111) orientation, exhibit an approximate (2x2) superstructure with respect to the Pt(111) and Ag(111) surface structure. In contrast, the α-Fe_2O_3(0001) surface is characterized by an approximate ($\sqrt{3}$x$\sqrt{3}$)R30° superstructure[13, 29] with extra satellite spots due to the biphase.[41-43] These differences can be utilized to separate the phases in dark-field LEEM imaging (Figure 2b-c), visualizing selectively the sample regions contributing to individual LEED spots. The different chemical composition between the inverse spinel and the corundum phases was indicated by the contrast in the XPEEM image at the Fe 3p peak. Initial and final chemical compositions of the oxide phases were determined by spatially resolved XPS (μ-XPS, Figure 2d-e) and XPEEM. Following the arguments used in the previous article[13], we call γ-Fe_2O_3 the Fe-oxide inverse spinel phase which is composed only by Fe^{3+} cations, as shown by the missing chemical contrast in XPEEM between this phase and α-Fe_2O_3. In contrast, an additional shoulder at the lower binding energy side of the Fe 3p XPS peak proves the presence of Fe^{2+} ions and indicates that the spinel structure is Fe_3O_4 which can be more or less stoichiometric (due to varying amounts of Fe vacancies).

While the Fe_3O_4 and α-Fe_2O_3 phases in mixed films are easily identified by the characteristic fingerprints in LEED and by the different chemical contrast at the Fe 3p peak (in XPEEM), the experimental identification of the γ-Fe_2O_3 phase is more complex. For this purpose, we prepared the films in two steps. In the first preparation step, we oxidized the initial Fe_3O_4 film at low temperature (T < 620 K, p_{O2}= 3×10^{-5} mbar). LEEM-IV and LEED of such a film differs significantly from the one of Fe_3O_4 indicating that a new spinel phase is formed. XPS spectra at the Fe 3p peak were also acquired. In the second step, UHV annealing up to T = 850 K induced the structural transformation from the spinel phase to α-Fe_2O_3. The annealing was stopped when the two oxide phases were seen to co-exist within the field of view. Spatially resolved XPS of the two oxide phases were measured under

identical instrumental conditions. Using the $\alpha\text{-Fe}_2\text{O}_3$ XPS spectra as reference, we could determine the stoichiometry of the spinel oxide by direct comparison. The absence of contrast in the local XPS spectra indicated that the two phases (spinel and corundum crystals) are Fe_2O_3 allotropes: therefore, we identify the spinel phase as $\gamma\text{-Fe}_2\text{O}_3$. Comparison with the spectra acquired immediately after the low temperature oxidation confirmed that the $\gamma\text{-Fe}_2\text{O}_3$ phase had already formed.

The focus of our experiments was the direct observation of the phase transformations between different iron oxides phases (Fe_3O_4, $\alpha\text{-Fe}_2\text{O}_3$ and $\gamma\text{-Fe}_2\text{O}_3$) under defined experimental conditions (e.g. temperature, oxygen pressure, substrate steps). As a measure for the reaction rates we took the velocity of the moving phase boundary between parent and reaction products. In all cases we selected conditions and areas where parent and product phases already co-existed on the sample, when the observation of the moving reaction front started. In this way we excluded the initial nucleation process. The front velocity $v_{boundary} = \Delta s_{boundary}/\Delta t$ was evaluated from sequences of LEEM images, as the average phase boundary displacement ($\Delta s_{boundary}$) that occurred in the time interval Δt. This procedure could also be applied while varying the temperature. Since the selection of areas of phase coexistence and of conditions for well-observable moving fronts was tedious, and the conditions for reaching such coexistence regions differed for the different phase transitions, the heating procedure was not identical for all experiments. This also led to varying starting points for the observation of front motion in terms of temperature and velocity for the various cases; therefore, no uniform "window of observability" for the front motion exists. In some cases the thermal sample drift forced to lower the heating rate in order to move the studied sample region back into the field of view by manual change of the manipulator mechanics. This caused a partially nonlinear behavior in the temperature ramping. However, since the individual LEEM frames were time-tagged and tied to the actual temperature, the temperature dependence of the velocities could be extracted with an estimated error below 20 %. Because of the complicated shape of many fronts to be described in Result section the fronts were smoothed before application of this procedure, and the determined motion is an average velocity. Nevertheless, in view of the large differences of velocities to be reported, this procedure confers a semi-quantitative view of the processes. And since the same procedures were applied while changing the temperature, these T-dependences are also significant.

The front velocity can be seen as a measure for the fraction δ of converted material per time, and therefore for the reaction rate. If $V = A\,d$ is the volume of the converted oxide film, with A being the converted surface area and d the film thickness, then the conversion rate is given by:

$$\frac{d\delta}{dt} \propto \frac{dV}{dt} = \frac{\partial A}{\partial t}d + \frac{\partial d}{\partial t}A \xrightarrow[d=const]{} \frac{d\delta}{dt} \propto \frac{\partial A}{\partial t}d = v\,L\,d$$

Here L is the width of the front. Consequently, in first approximation, the experimental front velocity v is proportional to the reaction rate $\frac{d\delta}{dt}$ (the sample thickness is assumed to be constant).

For a thermally activated reaction with constant rate-determining step we expect Arrhenius behavior:

$$v = v_0 \, e^{-\frac{E_A}{k_B T}}$$

where v_0 is the pre-exponential, E_A the activation energy, T the absolute temperature, and K_B the Boltzmann constant.

During the experiments, the "mixed" films were annealed under isobaric conditions (UHV, p_{O2} = 10^{-6} mbar, or p_{O2} = 3 10^{-5} mbar) and observed in real space. The compositions and structures of the iron oxide films were characterized before and after the experiments by LEEM, LEED, XPEEM and XPS, in order to differentiate between the "direct" Fe_3O_4 → α-Fe_2O_3 transformation and the solely "structural" γ-Fe_2O_3 → α-Fe_2O_3 conversion.

4   Results

An overview of the real time LEEM observations of the different phase transformations is given in Figure 3. For each transformation three snapshots during the annealing are shown together with the corresponding temperature and time of annealing. Whereas in the first three rows (Figure 3 a-c) the oxide film was annealed in UHV, the last two rows display the conversion under oxygen pressure (Figure 3 d-e). Depending on the electron energy the α-Fe_2O_3 phase appears bright (E_{kin} = 23, 24, 24, 20 eV in a), b), d) and e), respectively), but dark in c) at E_{kin} = 29 eV. The other phase in the images is Fe_3O_4 in b-e), except for a) where the dark area is γ-Fe_2O_3. The different crystalline phases were identified by LEEM/LEED and XPEEM/XPS as described before. All images in each sequence are drift-compensated and show the same surface region. As a guide to the eye, the position and shape of the initial boundary is inserted as a line in the following two images of the sequence. Clearly the structural transformations proceed by distinct movement of the phase boundary increasing the area of one type of crystalline phase, as already described in ref. [13]. The conversion always leads to an α-Fe_2O_3 phase, except for b) where Ag(111) instead of Pt(111) was used as support and α-Fe_2O_3 completely transformed into Fe_3O_4. The different behavior of the mixed film observed under the same experimental conditions (i.e. UHV annealing) on the two substrates is attributed to the fact that Fe can be dissolved in the Pt(111) support, but not in the Ag substrate, as discussed in detail in our previous work[13]. The sequences differ in both the time scale for the conversion (45 s in Figure 3a compared to 50 min in b) and the temperature range (T = 670-700 K for the oxidation in 3 10^{-5} mbar and T = 800-900 K in 10^{-6} mbar).

The sequences exhibit two main issues: the shape, and the velocity, of the fronts. In all cases we observed a rough and never a smooth or straight phase boundary; however, the scale of this corrugation differed considerably. Whereas the boundaries for the conversion on Ag(111) (Figure 3b) and the $Fe_3O_4 \rightarrow \alpha\text{-}Fe_2O_3$ transformation by annealing in UHV and 10^{-6}mbar on Pt(111) (Figure 3c+d) are rather smooth, the boundaries for the $\gamma\text{-}Fe_2O_3 \rightarrow \alpha\text{-}Fe_2O_3$ and the higher temperature range of $Fe_3O_4 \rightarrow \alpha\text{-}Fe_2O_3$ have a pronounced dendritic shape (Figure 3a+e). The obtained average front velocities vary over more than two orders of magnitude: In the two cases of pronounced dendritic shape, the velocity was about 100 nm/s; in contrast, the front motion in the other three cases was distinctly slower, in a range between 1 nm/s (transformation on Ag(111), Figure 3b) and about 10 nm/s.

Before we discuss the shape and velocity in more detail we want to point out that while the compositional transformation $Fe_3O_4 \rightarrow \gamma\text{-}Fe_2O_3$ has been investigated as well, it does not appear in Figure 3. The reason is that in contrast to the other cases, no transformation front was observed during this conversion, even though the image contrast was carefully optimized by choosing the electron energy with the maximum difference in electron reflectivity for the two phases. The intensity was seen to change homogeneously over the observation range. Consequently, the conversion must occur homogeneously, without visible phase boundary. Hence no front velocity could be evaluated.
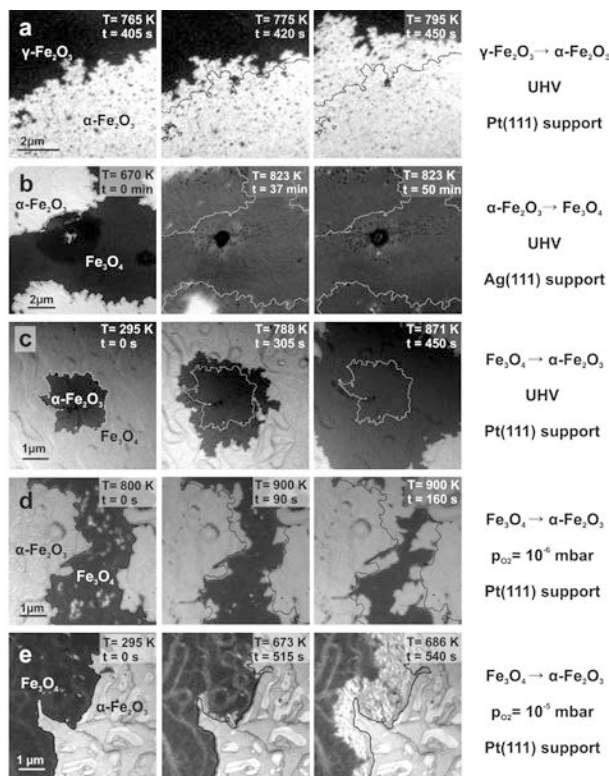
Figure 3: Overview of LEEM images of the observed transformations. Annealing in UHV (a-c) and in oxygen pressure (d: 10^{-6} mbar and e: 3 10^{-5} mbar). The different crystalline phases (α-Fe$_2$O$_3$, γ-Fe$_2$O$_3$ and Fe$_3$O$_4$) are labelled in the images. The contrast depends on the kinetic energy of the LEEM image (a: 23 eV, b: 24 eV, c: 29 eV, d: 24 eV, e: 20 eV). Pt(111) is used as support, except for b), where the film is supported by Ag(111). Temperature and time are indicated in the images.

4.1 Temperature dependences of average front motion

Figure 4 displays the temperature dependence of the average front velocities for the five conversions shown in Figure 3 in an Arrhenius plot. A wide variation in the reaction velocity is seen: from 1 nm/s for the reduction α-Fe$_2$O$_3$ → Fe$_3$O$_4$ observed on Ag(111) to more than 200 nm/s for the reverse reaction, i.e. the oxidation Fe$_3$O$_4$ → α-Fe$_2$O$_3$ on Pt(111) in an oxygen pressure of p=3x10^{-5} mbar. For most data sets the velocity depends exponentially on the inverse temperature to good approximation which suggests that a constant, thermally activated process dominates the rate of the slow step for boundary movement; an effective activation energy can then be obtained. A minor exception is the case of the conversion Fe$_3$O$_4$ → α-Fe$_2$O$_3$ by annealing in UHV for which the front velocity decreases at high temperature, indicating a change of the rate-determining step. A major difference of behavior was observed for the oxidation at 3 10^{-5} mbar (upper right of plot), for which sometimes even an acceleration of the boundary movement was observed at constant temperature. The T-dependent points, obtained after an induction period, are therefore much more uncertain than the others; nevertheless it is clear that not only a very different mechanism is at work, but also that it cannot be used to derive an activation energy.
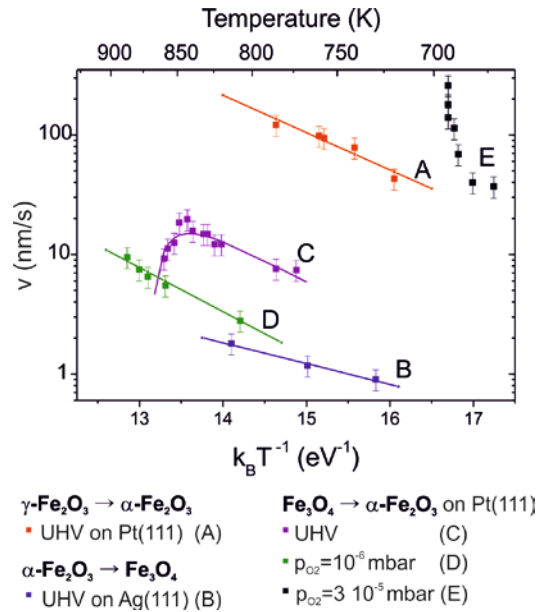
Figure 4: Arrhenius plot of the average front velocities for the transformations (i) γ-Fe₂O₃ → α-Fe₂O₃ in UHV (A: red curve), (ii) Fe₃O₄ → α-Fe₂O₃ in UHV (C: purple), p_{O2}=10⁻⁶ mbar (D: green), p_{O2}=3 10⁻⁵ mbar (E: black) and (iii) α-Fe₂O₃ → Fe₃O₄ in UHV (B: blue). The oxide film for the transformations (i) and (ii) were grown on Pt(111), whereas (iii) was grown on Ag(111). Linear fits are given by lines. Note that the behavior of Fe₃O₄ → α-Fe₂O₃ in p_{O2}=3 10⁻⁵ mbar (black squares) was very different, as described in the text; therefore no Arrhenius fit has been done there.

The parameters of an exponential fit $v = v_0 \exp(-E_A/k_B T)$ are listed in Table 1. In the case of the UHV annealing of Fe₃O₄ → α-Fe₂O₃ we used a sum of two exponential contributions, assuming additionally a reverse transformation: $v = v_{01} \exp(-E_{A1}/k_B T) - v_{02} \exp(-E_{A2}/k_B T)$. The fitting curves are included in Figure 3 as solid lines.

Substrate	Transformation	Slope (eV)	Intercept log(v₀)	Type of Transformation (XPS)
Pt(111)	**Fe₃O₄ → α-Fe₂O₃** (p_{O2} =10⁻⁶ mbar)	0.85+/-0.075	5.68+/-0. 43	Compositional Structural
	Fe₃O₄ → α-Fe₂O₃ (p_{O2} = UHV) Dominating low **T**	0.82 +/-0.087	6.08 +/- 0,53	Compositional Structural
	Fe₃O₄ → α-Fe₂O₃ (p_{O2} = UHV) Dominating high T	(4.3 +/-0.4)	(26 +/- 2)	Compositional Structural
	γ-Fe₂O₃ → α-Fe₂O₃ (p_{O2} = UHV)	0.7 +/- 0.1	6,5 +/- 0.43	Structural
Ag(111)	**α-Fe₂O₃ → Fe₃O₄** (p_{O2} = UHV)	0.40 +/-0.038	2.7+/- 0.25	Compositional Structural

Table 1: Fit parameters of Arrhenius plot in Figure 4: the transformations observed, the supporting substrates, and the pressure are indicated. The last column states the transformation type based on XPS characterization.

4.2 Influence of substrate defects and crystalline domains

Besides the absolute velocities and their temperature dependence, the shapes and the variations of the velocity along the fronts were in the focus of our study. Comparing Figure 3c and Figure 3d with Figure 3e, we note that the same reaction, namely $Fe_3O_4 \rightarrow \alpha\text{-}Fe_2O_3$ exhibits two different front morphologies: non-dendritic and dendritic. In the following, we characterize the local reaction kinetics for both growth modes. First, we consider the non-dendritic one. The reasons why the transformation boundary is not smooth, but rough, can be manifold. In the following, we study the influence of the substrate topography and of the crystalline defects, such as rotational domains at an example shown in Figure 5, where an $\alpha\text{-}Fe_2O_3$ domain is surrounded by Fe_3O_4. During the cleaning procedure of the Pt(111) single crystal support the atomic steps, which were always present due to a slight miscut, accumulated to a few 10's or even 100 nm wide step bunches, which appeared in the LEEM image as dark or bright thick lines, depending on the focus condition and local change of termination by oxygen adsorption. When the substrate step bunches are overgrown by an about 10 nm thick film, they are still visible; see thick lines marked by arrows in Figure 5a. Due to the threefold crystal symmetry, the Fe_3O_4 films exhibit two kinds of rotational domains with sizes from 100 nm to microns, rotated by 180° against each other. The size and the ratio of this surface fraction depend on the preparation conditions of the film and on the substrate morphology [33] and can be easily visualized as bright and black areas by dark field LEEM for the identical surface region (Figure 5b). As expected for a sixfold crystalline structure, the $\alpha\text{-}Fe_2O_3(0001)$ domain (in the center) is uniform and has no rotational domains. These two LEEM images were taken before the annealing in UHV which resulted in a conversion of Fe_3O_4 into $\alpha\text{-}Fe_2O_3$ (see also Figure 3c). The evolution of the growing $\alpha\text{-}Fe_2O_3$ domain is represented by the color-coded lines, which are taken every 20 s along the propagation border at an annealing temperature of around 785 K. The superposition of these lines with the LEEM images allows to correlate the step bunches and rotational domains with the shape of the front and the local velocity. As soon as the front approaches a step bunch (see lower left area in Figure 5a) the propagation is hindered and slows down, as can be seen in the smaller distances of subsequent borderlines. As a consequence, the transformation front takes on the shape of the step bunches, which are smooth and nearly straight. However, the step bunches do not completely block the propagation, as the front motion continues after a while (see extension in the red curve in the lower left of Figure 5a).
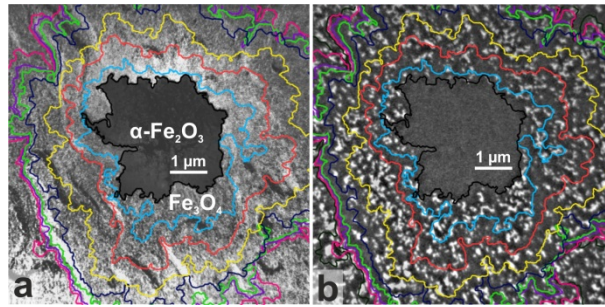
Figure 5: Influence of substrate step bunches (a) and of the initial rotational domains in the Fe₃O₄ phase on the front morphology and local front velocity. Colored lines represent the conversion boundary, taken every 20 s at 785 K in UHV. LEEM image (a) shows step bunches as dark and bright lines; dark field image (b) shows the rotational domain as bright and dark area. The front follows clearly the boundaries between rotational domains.

In contrast to the smooth front shape along step bunches, the front is rough in surface regions between the step bunches (for instance at the lower center in Figure 5a and b). The superposition of the borderlines with the rotational domains (Figure 5b) shows strong similarities between the curvature and the size of the rotational domains. Also, the position of the transformation front often coincides with the antiphase boundaries. A detailed examination shows that the front velocity is higher when the front crosses the center of a rotational domain, but lower at the antiphase boundary between neighboring rotational domains. The latter causes a temporary pinning of the front at the antiphase boundaries. Moreover, the velocity through both types of rotational domains is the same, which fits very well to the symmetry of the crystalline structures. As mentioned above the stacking sequences for the two types of Fe_3O_4 rotational domains are ABCABC and CBACBA, and are equivalent for the ABAB stacking of α-Fe_2O_3.

Summarizing these observations, both kinds of defects, step bunches of the substrate and antiphase boundaries, slow down the motion of the transformation front. This has also a direct effect on the shape of the front, which locally adopts the shape of the line defects: in our case smooth and elongated at step bunches and rough at the small rotational domains.

Though the effect is clearly visible in the LEEM images, the effect on the average front velocity is small, because the surface portions of step bunches and of antiphase domain boundaries are in the order of only a few percent.

4.3   Shape of the transformation fronts

In Figure 6 we depict the temporal development of the phase boundary (Figure 6a, c every 2s; Figure 6b every 1 s) during the oxidation of the mixed Fe_3O_4/ α-Fe_2O_3 film at an oxygen pressure of $3\ 10^{-5}$ mbar, i.e. for the case of unusual kinetics. The crystalline directions are shown in the inserted LEED

pattern, which corresponds exactly to the directions in the LEEM images. The bright, wide lines in the images are step bunches of the Pt(111) substrate, which are partially decorated by FeO defects and adsorbed oxygen during oxidation.

For a more detailed view, Figure 6b and Figure 6c show two zoomed-in regions, marked as yellow areas in Figure 6. The growing α-Fe$_2$O$_3$ front is characterized by highly dense branched dendritic structures which develop along specific orientations. Like in the case of UHV annealing, the dendritic branches follow the substrate step bunches (see e.g. area in Figure 6a marked by *); changes in the growth directions of the dendrites are also correlated to step bunches, which hinder the front motion (see branches marked with ** in Figure 6a).
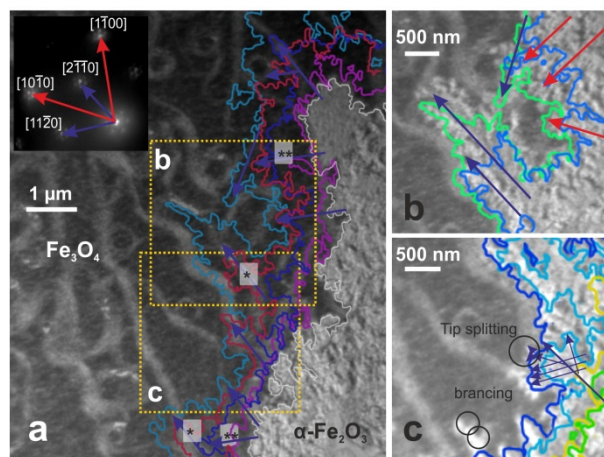
Figure 6: Front evolution at T= 700 K; p_{O2}=3 10^{-5} mbar. (a) Influence of preexisting step bunches on the dendrite directions, during the front evolution; (colored lines every 2 s). The crystalline orientations are indicated. E_k=20 eV. Fe$_3$O$_4$ (black), α-Fe$_2$O$_3$ (white). Bright lines in the Fe$_3$O$_4$ region are step bunches of the Pt(111) substrate. E_K=20 eV. (b) Zoomed area: dendrite branching and tip splitting during the α-Fe$_2$O$_3$ front growth. E_k =20 eV (colored lines every 1 s). (c) Zoomed area: details of the dendrite: growth directions are outlined. The front displacement (during same time interval of 2 s) along the < $1\bar{2}10$ > or equivalent crystalline directions (blue arrow) is almost twice as fast as in the <$1\bar{1}00$ > and equivalent directions (red). E_k=20 eV.

The dendrites develop mainly in the $[1\bar{2}10]$ -and equivalent- directions of the α-Fe$_2$O$_3$ crystal; some branches are also oriented along the $[1\bar{1}00]$ direction (blue and red arrows in Figure 6c, respectively). The growth of the branches along $[1\bar{2}10]$ is faster than in the $[1\bar{1}00]$ direction. With other words, the front velocity in the $[1\bar{2}10]$ direction is the highest, followed by the $[1\bar{1}00]$ direction. The velocities in all other directions are even smaller. This strong non-isotropic growth with distinct preferred direction leads to the observed dendritic growth.

During the α-Fe$_2$O$_3$ growth the main dendrite trunk splits into minor branches which are tilted against each other by a fixed angle of ±60°, corresponding to the equivalent crystalline orientations of the main dendrite.

Figure 3 c-e indicates that the shape of the Fe$_3$O$_4$ → α-Fe$_2$O$_3$ transformation front is affected by the oxygen pressure: rather smooth fronts for annealing in UHV and in a low oxygen pressure (1 10^{-6}

mbar), but dendritic in an oxygen pressure of 3 10^{-5} mbar. A possible explanation could be the influence of different defects in the film or in the support. This can be excluded by the following experiment, where the t transition between the two growth modes was observed for the identical iron oxide film and unchanged support topography.

The images in Figure 7 a-i show in *real time* how the transformation proceeds, while the O$_2$ pressure decreased from 3.0 10^{-5} mbar to 1.8 10^{-6} mbar. In the same time; the temperature of the sample slightly increased from 700 to 773 K.
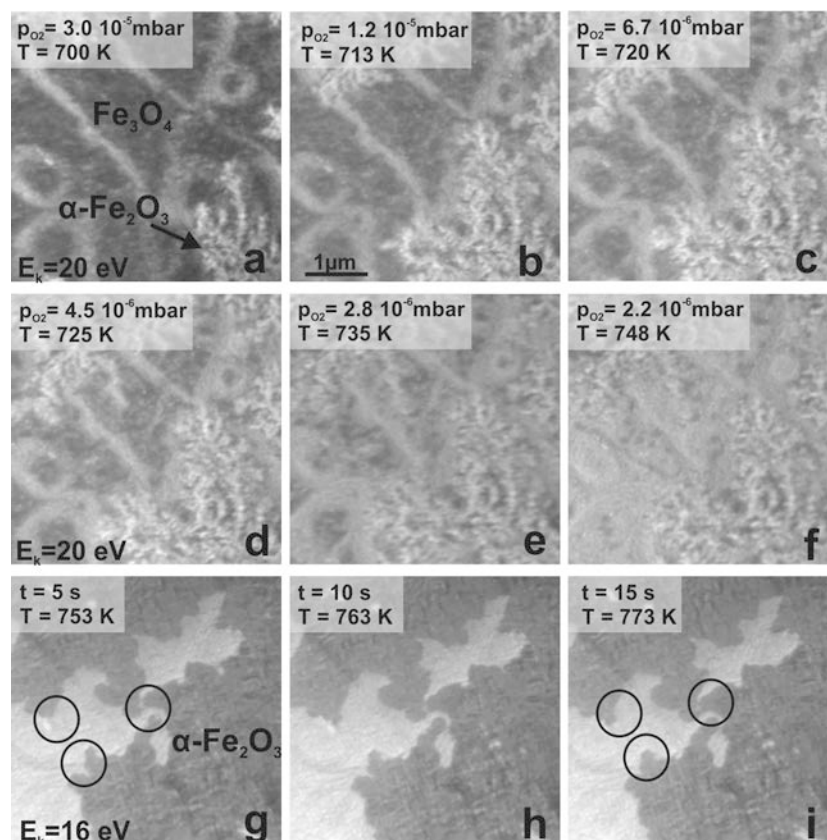
Figure 7: Evolution of oxidation dynamics when the pressure is lowered from 3 10^{-5} mbar (in a)) to 1.8 10^{-6} mbar (in i). Intensity change is visible in d-f). (a-c) Fe$_3$O$_4$ (dark) and α-Fe$_2$O$_3$ (bright). (d-e) change in the contrast of the Fe$_3$O$_4$ phase as consequence of the pressure decrease, E$_K$=20 eV; (g-i) front evolution at p = 1.8 10^{-6} mbar (constant); E$_k$ = 16 eV. The contrast changes between f and g due to the change in electron kinetic energy and focus. The energy was changed during acquisition to maintain the clear visualization of the phase boundary, almost invisible in (f)

During the initial pressure decrease the front velocity slowed down dramatically at p$_{O2}$≈ 6.7 10^{-6} mbar (Figure 7a-c), at almost constant temperature. Further decrease to p$_{O2}$ < 2.8 10^{-6} mbar (Figure 7 c-e) led to a change in the LEEM contrast which can be most likely related to a decrease of oxygen surface coverage. This can be explained by a structural change of the Fe$_3$O$_4$ termination, or even a change of the crystal phase from γ-Fe$_2$O$_3$ to Fe$_3$O$_4$, because the initial oxidation was done under the conditions, where γ-Fe$_2$O$_3$ was usually produced within 10 min (620 K, 3 10^{-5} mbar, see section 3). The oxidation has not completely stopped, as seen in the areas marked by circles in Figure 6g-i. However, the front

velocity drops by almost two orders of magnitude from v≈180 nm/s to v≈ 2.5 nm/s within Figure 7a-c. In the following, the morphology of the front changed from dendritic to rather smooth. In contrast to the dendritic growth, the front does not favor any specific growth direction. However, the boundary is still not smooth, most likely due to support and film defects as discussed above.

5   Discussion

In our experiments we have investigated the evolution of phase boundaries during four transformations: $Fe_3O_4 \rightarrow \gamma\text{-}Fe_2O_3$, $\gamma\text{-}Fe_2O_3 \rightarrow \alpha\text{-}Fe_2O_3$, $Fe_3O_4 \rightarrow \alpha\text{-}Fe_2O_3$ and $\alpha\text{-}Fe_2O_3 \rightarrow Fe_3O_4$. In the first one, $Fe_3O_4 \rightarrow \gamma\text{-}Fe_2O_3$, no reaction front was observable, therefore we exclude it from our analysis. In the other cases, we focused on two main aspects: the magnitudes and T-p dependences of the average velocities of the reaction fronts, and their shapes. The velocities of the fronts vary widely, depending on the type of transformation and/or the experimental conditions. A first classification can be done based on the front velocity: we have "fast" and "slow" transformations. The structural transformation $\gamma\text{-}Fe_2O_3 \rightarrow \alpha\text{-}Fe_2O_3$ in UHV and the $Fe_3O_4 \rightarrow \alpha\text{-}Fe_2O_3$ at $p_{O2}= 3 \cdot 10^{-5}$ mbar belong to the first class; the reduction $\alpha\text{-}Fe_2O_3 \rightarrow Fe_3O_4$ and the $Fe_3O_4 \rightarrow \alpha\text{-}Fe_2O_3$ observed in UHV and $p = 10^{-6}$ mbar belong to the second class.

The oxidation of $Fe_3O_4 \rightarrow \alpha\text{-}Fe_2O_3$ at $p= 3 \cdot 10^{-5}$ mbar is clearly set off from the other datasets: it is characterized by very high front velocity at low temperature, and the exponential temperature dependence is convoluted with a velocity increase even at constant temperature. Consequently these data have to be considered with caution: while we plotted them also in the Arrhenius plot, we refrain from a corresponding evaluation in terms of activation energy. They will be discussed separately. In the other cases we have obtained the apparent activation energies from exponential fits against the inverse temperature.

The purely structural transformation $\gamma\text{-}Fe_2O_3 \rightarrow \alpha\text{-}Fe_2O_3$ is much faster than the direct $Fe_3O_4 \rightarrow \alpha\text{-}Fe_2O_3$ reaction observed at low or vanishing O_2 pressures, as expectable. In the latter, long range Fe diffusion is required to adjust the Fe:O ration before the structural rearrangement can occur, while in the case of pure structural rearrangement point defects (Fe vacancies) are already available in the lattice and do not need to be created. Consequently the $\gamma \rightarrow \alpha$ transformation involves only the restacking of the oxygen planes and short range Fe diffusion, within the unit cell (also called diffusionless transformation).[10] Considering this difference it is surprising that the activation energies of the two reactions have similar values (0.7 eV and 0.85 eV). On the other hand the rates are set off strongly which is formally expressed in the different pre-exponentials. The much faster rate of the purely structural conversion suggests that the closeness of the apparent energies is

coincidental and the higher rate is due to a larger density of reactive centers for this simple conversion.

To discuss the direct $Fe_3O_4 \rightarrow \alpha\text{-}Fe_2O_3$ transformation in UHV first, we recall that Fe vacancies need to be created by removal of Fe atoms, most likely close to the phase boundary. Unfortunately the lack of temporal resolution in XPEEM made it impossible to check for the possible creation of a region characterized by an Fe concentration gradient (different stoichiometry than Fe_3O_4) during the reaction. The lack of contrast in the images obtained by static acquisition (i.e. after interrupting the transformation and quenching the sample down to about RT) suggests that this boundary is narrower than the spatial resolution of the XPEEM, or it disappears during the quenching before taking the XPEEM data. We cannot exclude that during conversion there is some change of the Fe:O ratio in the structurally Fe_3O_4 –like regions, since stoichiometric and non-stoichiometric magnetite, as well as maghemite, have all the same crystal structure and therefore the same structure in the LEED pattern. However, the electron reflectivity differs significantly between Fe_3O_4 and $\gamma\text{-}Fe_2O_3$ at certain energies, so the expected contrast in LEEM should reveal an intermediate $\gamma\text{-}Fe_2O_3$ phase. Because our LEEM data do not show such a contrast, a $\gamma\text{-}Fe_2O_3$ phase region, if it exists in an area in front of the boundary, is smaller than the lateral LEEM resolution in these experiments (approx. 20 nm) and therefore not visible for us. Additionally, we can exclude that maghemite forms as stable product under these conditions.

The oxidation processes of $Fe_3O_4 \rightarrow \alpha\text{-}Fe_2O_3$ performed under vanishing and small oxygen pressure (up to some 10^{-6} mbar) have similar activation energies, suggesting the same rate-determining process. In both cases the stoichiometry is adjusted by Fe diffusion in the (111) direction, and indeed the found activation energy agrees well with the published value for bulk oxidation which is dominated by Fe diffusion [32]. Under negligible oxygen supply via the surface Fe has to disappear to decrease the Fe/O ratio, and we have given evidence that Fe diffuses most likely into the Pt substrate [13] where it might form a subsurface Fe-Pt alloyed layer [44]. At $p_{O2}=1\ 10^{-6}$ there is also Fe diffusion to the surface of the film, where Fe is oxidized. The progressive decrease of the front velocity in UHV in the high temperature range can be understood as due to the decrease of oxygen surface concentration by activation of oxygen desorption, as already discussed in [13] . In this case, the reduction of the observed total rate for the transformation of Fe_3O_4 into $\alpha\text{-}Fe_2O_3$ might be attributed to partial reconversion of $\alpha\text{-}Fe_2O_3$ into Fe_3O_4. Under $p_{O2} = 1\ 10^{-6}$ mbar the front slow-down is not observed in the investigated temperature range, suggesting that adsorbing O from the gas phase prevents the decrease of O surface concentration. One might also suggest that the slowdown is due to a decrease of Fe dissolution in Pt or to the saturation of the Fe concentration in the sub-surface Fe-Pt layer. However, this would only be possible if the dissolution of Fe in Pt were

exothermic which certainly is not the case. Indeed, studies on the Fe-Pt system [44, 45] show that UHV annealing at T > 850 K induced the bulk diffusion of Fe into a Pt single crystal.

If we assume that the rate decrease under O_2 pressure is due to O_2 desorption, the dataset can be used to estimate the desorption energy of O_2, yielding in a very high value around 4 eV. This fits well an also high activation energy for oxygen diffusion in Fe_3O_4 and α-Fe_2O_3, respectively of 264 kJ/mol [46] (corresponding to 2.74 eV) and 4.05 kJ/mol [47] (corresponding to 4.1 eV). Our high activation energy might then also be explained by oxygen desorption from the Fe_3O_4(111) surface, the activation energy of which was calculated to be 3.5 eV [48]. Oxygen desorption from the subsurface region of the biphase terminated α-Fe_2O_3 thin film under similar experimental conditions was reported very recently.[49] However, we do not put emphasis on this exact value due to the limited range and the scatter of the data.

A puzzling aspect of these data is that the UHV conversion is distinctly faster than that under small oxygen pressure, and that the rate decrease of the former at higher T brings its rate down to the lower one under oxygen. The simplest model for these conditions is that under UHV only one path, diffusion into the Pt substrate, contributes (i.e. the chemical reaction 3 Fe_3O_4 $\rightarrow$ 4 Fe_2O_3 + Fe), while under oxygen there is also a contribution of Fe diffusion to the surface and reaction with oxygen there (i.e. the reaction 2 Fe_3O_4 + O $\rightarrow$ 3 Fe_2O_3). However, if these two possible paths were independent, the 2-path situation should lead to faster reaction than the 1-path. Alternatively, the two paths can compete with each other, as they act in the opposite directions, under two opposite Fe concentration gradients: one process tends to accumulate Fe at the surface, the other at the oxide/substrate interface. Following Fick's first law of diffusion, the Fe flux is directly proportional to the Fe gradient within the oxide film (from the surface towards the support interface). If this gradient is decreased by the oxidation process and concomitant reduction of Fe concentration at the surface, then the Fe diffusion into the bulk is reduced. Consequently, the net effect of these two diffusive processes is to reduce the effective flux of Fe cations from the film. This can explain why there is a lower reaction rate for Fe_3O_4 $\rightarrow$ α-Fe_2O_3 transformation during the annealing in p_{O2}=10^{-6} mbar compared to the UHV case. Moreover, it could be that the internal structure of the film is different in the two situations.

For oxide films on Ag(111) we observed the reducing reaction α-Fe_2O_3 $\rightarrow$ Fe_3O_4 and the corresponding front motion. We notice that the found activation energy of the process is much lower than for the reverse transformation (Fe_3O_4 $\rightarrow$ α-Fe_2O_3) and even more so than that expected for oxygen desorption (3.5 eV [48]), O diffusion in the oxide film (2.74 eV [46]) and formation of a subsurface O layer in the Ag substrate ($\approx$1 eV as calculated in [50]). Moreover, the range of rates is distinctly lower which formally is expressed in a lower pre-exponential factor. This aggravates the

problem encountered in the interpretation of the reaction on films on a Pt substrate where, as discussed above, two parallel paths appear to be slower than one. A similar conundrum appears now with inclusion of the reverse reaction on Ag-backed films. Since here the substrate cannot participate as source or sink of Fe, the reaction must proceed by oxygen desorption only, followed by Fe diffusion into the film. The much lower T-dependence shows that the latter cannot be the rate-determining step, which would be compatible with the overall low rates. If the slow step would be oxygen desorption, an even larger activation energy would be expected. So we conclude that the slow step must be different here. Without additional information, e.g., on possible changes in a narrow range at the boundary, we cannot give an explanation here. We think that the observed behavior is sufficiently interesting to be reported as such.

The real oddball reaction is the "high pressure" oxidation reaction. It not only shows very fast front movements at low temperature, but also complicated kinetics with an induction period and isothermal acceleration; the latter makes it difficult to give a reliable T-dependence, but the velocity is clearly very much higher than for all the other reactions. The clear connection to the strong dendritic morphology of the front which we have demonstrated suggests that the film surface has a different structure or possibly even corresponds to a different phase under these conditions (see also the following discussion of these changes). Unfortunately our spatial and temporal XPEEM resolution is insufficient to gain better insight into the fine-grained stoichiometry here. This remains a challenge for further work.

Focusing on the front shapes, we can identify two morphologic regimes: dendritic and non-dendritic. Using our first classification, we see that the reactions occurring with a dendritic front are the "fast" reactions ($\gamma \rightarrow \alpha$-$Fe_2O_3$ transformation and high pressure $Fe_3O_4 \rightarrow \alpha$-$Fe_2O_3$ oxidation), while the "slow" reactions are characterized by a non-dendritic front. Analyzing in detail the front shape during UHV annealing, we found two main factors influencing the local reaction velocity: the front is slowed by step bunches of the substrate and anti-phase domain boundaries in the Fe_3O_4 phase. However their effect on the front roughness is opposite: step bunches cause a straightening of the front, while the rotational domain boundaries cause its roughening.

The influence of the anti-phase domain boundaries on the reaction velocity might be explained considering that they are defects in the internal structure of the Fe_3O_4 phase. Anti-phase domain boundaries are regions where two different crystalline stackings interface (for instance ABCABC||ACBACB). Consequently the domain walls are rich of defects such as stacking faults, in-plane dislocations and vacancies and might hinder the atomic movements needed for the transformation. In addition to this first point, it is necessary to remember that the α-Fe_2O_3 island

grows by enlargement of one rotational domain (for instance ABABAB): at each domain boundary in the Fe_3O_4 film the restacking of the oxygen plane has to switch between the two "equivalent" restacking mechanisms and this may also contribute to the observed local slowing down of the reaction front. Other factors, not considered in the present work, might also change the local rate of the reaction, such as the presence of dewetted areas in the film, dislocations or varying local film thickness.

The formation of islands with dendritic shape can be explained by the model of diffusion limited aggregation (DLA [51, 52]). Dendrites were observed in crystal growth, for instant Pt or Ag homoepitaxy [53, 54] or Ag/Pt(111) [55, 56], and are explained there by the growth process: a random walk of adatoms, hitting an existing 2D island at an arbitrary site and stick just there, because of reduced mobility along the step edge. A well-known example in 3-dimension is the formation of snowflakes. Dendritic nano-structured α-Fe_2O_3 crystals have been synthesized by [57, 58] from liquid solutions. *Bharathi et al.* and *Cao et al.* observed that the branches follow the favorite $[1\bar{1}00]$ (and equivalent) growth direction; they attributed this to the maximization of the non-polar $(1\bar{1}00)$ and equivalent planes. However, this argument cannot be applied to our experiments, which show the contrary: the growth in the $[1\bar{2}10]$ direction is faster than in the $[1\bar{1}00]$ direction.

Moreover, in our case the transformation does not involve a real long distance diffusion process but rather the hopping of atoms from one coordination type to another. Therefore, in this case, the anisotropy causing the dendrite formation might be related to the hopping probability of the atoms in the new structural configuration. The reason for the difference might be that in our case the α-Fe_2O_3 crystal does not grow from liquid solution, but from a solid (Fe_3O_4) and thus with a different kind of growth front. The observed anisotropy might depend on the atomic structure of the α-$Fe_2O_3||Fe_3O_4$ interface along these two crystallographic directions; unfortunately we do not have experimental information on the atomic structure of these interfaces.

The smoothing of the front observed by lowering the oxygen pressure (Figure 6) is associated with a strong slowdown of the reaction rate despite an (inadvertent) concomitant increase of temperature. Usually, smooth fronts are thermodynamically more favored than rough fronts. Therefore, the observed transition might be the consequence of a change in the oxidation regime, from conditions far from thermodynamical equilibrium (fast oxidation at 10^{-5} mbar) to near equilibrium conditions (slow transformation at lower pressure). We attribute the transition to the change in the oxidation pressure from $3 \; 10^{-5}$ to $1.8 \; 10^{-6}$ mbar rather than to the temperature change, for the following reasons. First, the front velocity decreases by two order of magnitude by decreasing the pressure at almost constant temperature ($\Delta T= 13$ K at the most relevant step between Figure 6a and Figure 6b); if the T change would be governing it should increase. Secondly, dendrites develop in the

temperature range between 650 K and 700 K in p_{O2}= 3 10^{-5} mbar. On the other hand, we never observed dendrite development in the "low pressure growth" (for instance during UHV annealing from RT to 900 K) in the same temperature range, which should be the case if the transformation temperature was the parameter determining the transformation regime.

We would like to deepen our discussion of the "anomalous" behavior of the oxidation front at p_{O2}= 3 ×10^{-5} mbar. One possible scenario would be that at the used conditions for the transformation at 3×10^{-5} mbar and above 650 K, the Fe_3O_4 converts into γ-Fe_2O_3, at least in the top-most layers. This γ-layer transforms fast and with dendritic shape to α-Fe_2O_3 as observed in UHV for $\gamma \rightarrow \alpha$. When the O_2 pressure is reduced the γ-Fe_2O_3 converts back to Fe_3O_4 (white areas in Fig.6 g-i). This γ-phase (produced within a few minutes at 3×10^{-5} mbar of oxygen and 650 K) is therefore not stable, whereas the γ-phase produced slowly (by 10 min reaction) is stable: cooling down first in oxygen (down to 450 K) and subsequently to RT in UHV changes neither structure nor composition (in XPS no Fe^{2+}). The possible reason for this difference could be that in the latter case the entire film thickness is converted and therefore stable, whereas in the former only the top-most layers are converted and are therefore unstable.

6   Conclusions

We have presented an extensive study on the phase transformations between three Fe oxide phases (α-Fe_2O_3, γ-Fe_2O_3, Fe_3O_4), based on the combination of real time imaging, chemical, and structural characterization. Particular attention was laid on the developing reaction fronts and their morphology and velocity. Our experiments show that the structural transformations from inverse spinel to corundum ($Fe_3O_4 \rightarrow \alpha$-$Fe_2O_3$ or γ-$Fe_2O_3 \rightarrow \alpha$-$Fe_2O_3$) and the reverse transformation (α-$Fe_2O_3 \rightarrow Fe_3O_4$) are heterogeneous processes (i.e. with reaction fronts), while the purely compositional change $Fe_3O_4 \rightarrow \gamma$-$Fe_2O_3$ is a homogeneous process. We find two classes of propagating reaction boundaries: (i) slow fronts (1-10 nm/s) with a rather smooth shape for the combined structural and compositional transitions ($Fe_3O_4 \rightarrow \alpha$-$Fe_2O_3$ and reverse) and (ii) fast fronts (100 nm/s) with dendritic shape for the purely (or mainly) structural transition (γ-$Fe_2O_3 \rightarrow \alpha$-$Fe_2O_3$ and/or non-stoichiometric magnetite $Fe_{3-\delta}O_4 \rightarrow \alpha$-$Fe_2O_3$). The front shapes are influenced by defects in the support and oxide film such as step bunches and rotational domains. We identify Fe diffusion, oxygen adsorption, and oxygen desorption as processes involved in the various transformations. From the temperature dependences of the front velocities we derive effective activation energies, which are in most cases related to the Fe diffusion within the oxide film. However, some observed details can be not fully explained at present and deserve further investigations: e.g. what is the reason for the slowdown at

higher temperature of the transformation in UHV, why is the reaction rate lower in 10^{-6} mbar of oxygen than in UHV and why is the activation energy for the inverse process on Ag(111) so low?

References

[1] M. Sugimoto, The Past, Present, and Future of Ferrites, Journal of the American Ceramic Society, 82 (1999) 269-280.

[2] D.S. Mathew, R.-S. Juang, An overview of the structure and magnetism of spinel ferrite nanoparticles and their synthesis in microemulsions, Chemical Engineering Journal, 129 (2007) 51-65.

[3] Q.A. Pankhurst, J. Connolly, S. Jones, J. Dobson, Applications of magnetic nanoparticles in biomedicine, Journal of physics D: Applied physics, 36 (2003) R167.

[4] R.M. Cornell, U. Schwertmann, Introduction to the Iron Oxides, in: The Iron Oxides, Wiley-VCH Verlag GmbH & Co. KGaA, 2004, pp. 1-7.

[5] D. Sun, S. Senz, D. Hesse, Crystallography, microstructure and morphology of $Mg_4Nb_2O_9$/MgO and $Mg_4Ta_2O_9$/MgO interfaces formed by topotaxial solid state reactions, Journal of the European Ceramic Society, 26 (2006) 3181-3190.

[6] R. Röttger, H. Schmalzried, Chemical kinetics at solid/solid interfaces, Solid State Ion., 150 (2002) 131-141.

[7] G.S. Rohrer, Influence of interface anisotropy on grain growth and coarsening, Annu. Rev. Mater. Res., 35 (2005) 99-126.

[8] W. Jo, D.-Y. Kim, N.-M. Hwang, Effect of Interface Structure on the Microstructural Evolution of Ceramics, Journal of the American Ceramic Society, 89 (2006) 2369-2380.

[9] S.Y. Chung, S.J.L. Kang, Effect of dislocations on grain growth in strontium titanate, Journal of the American Ceramic Society, 83 (2000) 2828-2832.

[10] H. Schmalzried, Chemical kinetics of solids, VCH, Weinheim ; New York, 1995.

[11] R. Benedek, D. Seidman, C. Woodward, The effect of misfit on heterophase interface energies, Journal of Physics: Condensed Matter, 14 (2002) 2877.

[12] D. Hesse, P. Werner, R. Mattheis, J. Heydenreich, Interfacial reaction barriers during thin-film solid-state reactions: The crystallographic origin of kinetic barriers at the NiS2/Si(111) interface, Appl. Phys. A, 57 (1993) 415-425.

[13] F. Genuzio, A. Sala, T. Schmidt, D. Menzel, H.-J. Freund, Interconversion of α-Fe_2O_3 and Fe_3O_4 Thin Films: Mechanisms, Morphology, and Evidence for Unexpected Substrate Participation, The Journal of Physical Chemistry C, (2014).

[14] R. Wichtendahl, R. Fink, H. Kuhlenbeck, D. Preikszas, H. Rose, R. Spehr, P. Hartel, W. Engel, R. Schlögl, H.-J. Freund, SMART: An aberration-corrected XPEEM/LEEM with energy filter, Surf. Rev. Lett., 5 (1998) 1249-1256.

[15] T. Schmidt, U. Groh, R. Fink, E. Umbach, O. Schaff, W. Engel, B. Richter, H. Kuhlenbeck, R. Schlögl, H.-J. Freund, XPEEM with energy-filtering: advantages and first results from the SMART project, Surf. Rev. Lett., 9 (2002) 223-232.

[16] R. Fink, M. Weiss, E. Umbach, D. Preikszas, H. Rose, R. Spehr, P. Hartel, W. Engel, R. Degenhardt, R. Wichtendahl, SMART: a planned ultrahigh-resolution spectromicroscope for BESSY II, J. Electron Spectrosc. Relat. Phenom., 84 (1997) 231-250.

[17] T. Schmidt, A. Sala, H. Marchetto, E. Umbach, H.-J. Freund, First experimental proof for aberration correction in XPEEM: Resolution, transmission enhancement, and limitation by space charge effects, Ultramicroscopy, 126 (2013) 23-32.

[18] T. Schmidt, H. Marchetto, P.L. Lévesque, U. Groh, F. Maier, D. Preikszas, P. Hartel, R. Spehr, G. Lilienkamp, W. Engel, R. Fink, E. Bauer, H. Rose, E. Umbach, H.J. Freund, Double aberration correction in a low-energy electron microscope, Ultramicroscopy, 110 (2010) 1358-1361.

[19] B. Luerßen, J. Janek, S. Günther, M. Kiskinova, R. Imbihl, Microspectroscopy at a moving reduction front in zirconia solid electrolyte, Phys. Chem. Chem. Phys., 4 (2002) 2673-2679.

[20] H.H. Rotermund, S. Nettesheim, A. von Oertzen, G. Ertl, Observation of surface diffusion of adsorbates on metal surfaces by photoemission electron microscopy (PEEM), Surf. Sci., 275 (1992) L645-L649.

[21] H. Marbach, G. Lilienkamp, H. Wei, S. Günther, Y. Suchorski, R. Imbihl, Ordered phases in alkali redistribution during a catalytic surface reaction, Phys. Chem. Chem. Phys., 5 (2003) 2730-2735.

[22] H. Marbach, S. Günther, B. Luerssen, L. Gregoratti, M. Kiskinova, R. Imbihl, Selforganization of alkali metal on a catalytic metal surface, Catalysis letters, 83 (2002) 161-164.

[23] M. Monti, B. Santos, A. Mascaraque, O. Rodríguez de la Fuente, M. Niño, T. Mentes, A. Locatelli, K. McCarty, J. Marco, J. de la Figuera, Oxidation pathways in bicomponent ultrathin iron oxide films, The Journal of Physical Chemistry C, 116 (2012) 11539-11547.

[24] S. Günther, T.O. Menteş, M.A. Niño, A. Locatelli, S. Böcklein, J. Wintterlin, Desorption kinetics from a surface derived from direct imaging of the adsorbate layer, Nat Commun, 5 (2014).

[25] S. Nettesheim, A. Von Oertzen, H. Rotermund, G. Ertl, Reaction diffusion patterns in the catalytic CO-oxidation on Pt(110): Front propagation and spiral waves, The Journal of chemical physics, 98 (1993) 9977-9985.

[26] R.M. Cornell, U. Schwertmann, Crystal Structure, in: The Iron Oxides, Wiley-VCH Verlag GmbH & Co. KGaA, 2004, pp. 9-38.

[27] R.M. Cornell, U. Schwertmann, Thermodynamics of the Fe-O_2-H_2O System, in: The Iron Oxides, Wiley-VCH Verlag GmbH & Co. KGaA, 2004, pp. 185-199.

[28] R.M. Cornell, U. Schwertmann, Transformations, in: The Iron Oxides, Wiley-VCH Verlag GmbH & Co. KGaA, 2004, pp. 365-407.

[29] W. Weiss, W. Ranke, Surface chemistry and catalysis on well-defined epitaxial iron-oxide layers, Progress in Surface Science, 70 (2002) 1-151.

[30] X.-S. Yang, S. Sun, X.-L. Wu, E. Ma, T.-Y. Zhang, Dissecting the Mechanism of Martensitic Transformation via Atomic-Scale Observations, Sci. Rep., 4 (2014).

[31] U. Colombo, F. Gazzarini, G. Lanzavecchia, Mat. Sci. Eng., 2 (1967) 125-125.

[32] P.S. Sidhu, R.J. Gilkes, A.M. Posner, Mechanism of the low temperature oxidation of synthetic magnetites, Journal of Inorganic and Nuclear Chemistry, 39 (1977) 1953-1958.

[33] C. Carter, Y. Simpson, Thin-Film Reactions, Berichte der Bunsengesellschaft für physikalische Chemie, 90 (1986) 676-680.

[34] D. Hesse, H. Bethge, Solid state reactions for the epitaxial growth of spinel films, Journal of Crystal Growth, 65 (1983) 69-76.

[35] S. Kachi, K. Momiyama, S. Shimizu, An Electron Diffraction Study and a Theory of the Transformation from γ-Fe_2O_3 to α-Fe_2O_3, J. Phys. Soc. Jpn., 18 (1963) 106-116.

[36] G.C. Bye, G.T. Simpkin, Influence of Cr and Fe on Formation of α-Al_2O_3 from γ-Al_2O_3, Journal of the American Ceramic Society, 57 (1974) 367-371.

[37] R.B. Bagwell, G.L. Messing, P.R. Howell, The formation of α-Al_2O_3 from θ-Al_2O_3: The relevance of a "critical size" and: Diffusional nucleation or "synchro-shear"?, Journal of Materials Science, 36 (2001) 1833-1841.

[38] Y. Watanabe, K. Ishii, Geometrical consideration of the crystallography of the transformation from α-Fe_2O_3 to Fe_3O_4, physica status solidi (a), 150 (1995) 673-686.

[39] M.F. Yan, Grain growth in Fe_3O_4, Journal of the American Ceramic Society, 63 (1980) 443-447.

[40] A. Sala, H. Marchetto, Z.-H. Qin, S. Shaikhutdinov, T. Schmidt, H.-J. Freund, Defects and inhomogeneities in Fe_3O_4(111) thin film growth on Pt(111), Phys. Rev. B, 86 (2012) 155430.

[41] N. Condon, F. Leibsle, A. Lennie, P. Murray, D. Vaughan, G. Thornton, Biphase ordering of iron oxide surfaces, Phys. Rev. Lett., 75 (1995) 1961.

[42] R.J. Lad, V.E. Henrich, Structure of α-Fe_2O_3 single crystal surfaces following Ar+ion bombardment and annealing in O_2, Surf. Sci., 193 (1988) 81-93.

[43] C.H. Lanier, A.N. Chiaramonti, L.D. Marks, K.R. Poeppelmeier, The Fe_3O_4 origin of the "Biphase" reconstruction on α-Fe_2O_3(0001), Surf. Sci., 603 (2009) 2574-2579.

[44] D.I. Jerdev, B.E. Koel, Fe deposition on Pt(111): a route to Fe-containing Pt–Fe alloy surfaces, Surf. Sci., 513 (2002) L391-L396.

[45] T.-Y. Lee, S. Sarbach, K. Kuhnke, K. Kern, Growth and surface alloying of Fe on Pt(111), Surf. Sci., 600 (2006) 3266-3273.

[46] A.G. Crouch, J. Robertson, Creep and oxygen diffusion in magnetite, Acta Metallurgica et Materialia, 38 (1990) 2567-2572.

[47] K.P.R. Reddy, A.R. Cooper, Oxygen Diffusion in MgO and α-Fe_2O_3, Journal of the American Ceramic Society, 66 (1983) 664-666.

[48] D. Santos-Carballal, A. Roldan, R. Grau-Crespo, N.H. de Leeuw, A DFT study of the structures, stabilities and redox behaviour of the major surfaces of magnetite Fe_3O_4, Phys. Chem. Chem. Phys., (2014).

[49] H. Qiu, V. Staemmler, H. Kuhlenbeck, E. Bauer, H.-J. Freund, Weak thermal reduction of biphase Fe_2O_3(0001) films grown on Pt(111): Sub-surface Fe^{2+} formation, Surf. Sci., 641 (2015) 30-36.

[50] W.-X. Li, C. Stampfl, M. Scheffler, Subsurface oxygen and surface oxide formation at Ag(111): A density-functional theory investigation, Phys. Rev. B, 67 (2003) 045408.

[51] T.t. Witten, L. Sander, Diffusion-limited aggregation, Phys. Rev. B, 27 (1983) 5686.

[52] T. Witten Jr, L.M. Sander, Diffusion-limited aggregation, a kinetic critical phenomenon, Phys. Rev. Lett., 47 (1981) 1400.

[53] M. Bott, T. Michely, G. Comsa, The homoepitaxial growth of Pt on Pt(111) studied with STM, Surf. Sci., 272 (1992) 161-166.

[54] E. Cox, M. Li, P.-W. Chung, C. Ghosh, T. Rahman, C.J. Jenks, J.W. Evans, P.A. Thiel, Temperature dependence of island growth shapes during submonolayer deposition of Ag on Ag(111), Phys. Rev. B, 71 (2005) 115414.

[55] H. Brune, H. Röder, K. Bromann, K. Kern, J. Jacobsen, P. Stoltze, K. Jacobsen, N. Jens, Anisotropic corner diffusion as origin for dendritic growth on hexagonal substrates, Surf. Sci., 349 (1996) L115-L122.

[56] H. Brune, H. Röder, K. Bromann, K. Kern, Kinetic processes in metal epitaxy studied with variable temperature STM: Ag/Pt(111), Thin Solid Films, 264 (1995) 230-235.

[57] S. Bharathi, D. Nataraj, K. Senthil, M. Yoshitake, Shape-controlled synthesis of α-Fe_2O_3 nanostructures: engineering their surface properties for improved photocatalytic degradation efficiency, J Nanopart Res, 15 (2012) 1-13.

[58] M. Cao, T. Liu, S. Gao, G. Sun, X. Wu, C. Hu, Z.L. Wang, Single-Crystal Dendritic Micro-Pines of Magnetic α-Fe_2O_3: Large-Scale Synthesis, Formation Mechanism, and Properties, Angewandte Chemie International Edition, 44 (2005) 4197-4201.